# Photodissociation spectroscopy and dynamics of the $N_2O_2^-$ anion

David L. Osborn, David J. Leahy,[a] Douglas R. Cyr,[b] and Daniel M. Neumark
*Department of Chemistry, University of California, Berkeley, California, 94720 and Chemical Sciences Division, Lawrence Berkeley Laboratory, Berkeley, California 94720*

(Received 12 September 1995; accepted 27 December 1995)

The spectroscopy and dissociation dynamics of the $N_2O_2^-(C_{2v})$ anion have been investigated using the technique of fast ion beam translational spectroscopy. A newly developed pulsed supersonic discharge source is described for the production of internally cold $N_2O_2^-$. A structured absorption band beginning near 580 nm is observed, and is assigned to the $\tilde{B}(^2A_2)\leftarrow\tilde{X}(^2B_2)$ transition with the aid of *ab initio* calculations. Two dissociation channels from the upper state are observed: (1) $O^-+N_2O$ and (2) $NO^-+NO$. Translational energy and angular distributions are measured for both channels at several excitation energies. The translational energy distribution for channel (1) at 570 nm shows resolved structure corresponding to $N_2O$ vibrational excitation. The translational energy distributions for channel (1) are reasonably well described by prior distributions, indicating this channel results from dissociation from the $N_2O_2^-$ ground electronic state. In contrast, channel (2) appears to result from dissociation on a repulsive excited electronic state. From the translational energy distributions for channel (1), we obtain the bond dissociation energy and heat of formation (at 0 K) for $N_2O_2^-$: $D_0(O\text{–}N_2O)=1.40\pm0.03$ eV and $\Delta H^0_{f,0}(N_2O_2^-)=0.58\pm0.04$ eV. © *1996 American Institute of Physics.* [S0021-9606(96)00713-8]

## I. INTRODUCTION

In recent years, photodissociation experiments have been performed on a considerable number of neutral molecules and positive ions. These experiments have proved invaluable in understanding the electronic spectroscopy and dissociation dynamics of these species. In contrast, there have been relatively few photodissociation studies of negative ions. Anion photodissociation is problematic because, in most negative ions, bond dissociation energies are higher than the threshold for electron detachment, so that the dissociative anion state one might hope to access is generally embedded in the neutral $+e^-$ continuum. Nonetheless, photodissociation studies have been carried out on open shell anions such as $Cl_2^-$[1] or $CO_3^-$[2,3] for which the smallest bond dissociation energy is less than the electron binding energy, and on species such as $O_3^-$[4] and $O_4^-$[5,6] in which photodissociation occurs at energies well above the threshold for electron detachment. In this paper, we use a fast ion beam experiment to investigate the photodissociation spectroscopy and dynamics of the $N_2O_2^-$ anion, an open-shell species with a high electron binding energy.

The work presented here is motivated by recent results on the gas phase spectroscopy and dynamics of the $N_2O_2^-$ anion. In a photoelectron spectroscopy study, Posey and Johnson[7] demonstrated the existence of three distinct isomers of $N_2O_2^-$ which can each be prepared selectively in the gas phase by electron impact on a supersonic expansion of different gases. They characterized these isomers as: (I) $O_2^-\cdot N_2$, from $O_2$ seeded in $N_2$; (II) $NNO_2^-$, from neat $N_2O$; and (III) $NO^-\cdot NO$, from NO seeded in argon. Their results indicated that isomer (I) is a weakly bound cluster, while the other two isomers are more strongly bound species. Their proposed $C_{2v}$ structure for isomer (II) is supported by subsequent *ab initio* calculations,[8] which also suggest that isomer (III) has a *trans*-$ONNO^-$ structure. Furthermore, several matrix isolation studies[9–12] have identified a $C_{2v}$ structure consistent with isomer (II), and a species of the form $ONNO^-$ which most likely represents isomer (III).

The existence of multiple isomers is particularly interesting in light of isotopic labeling experiments on the ion-molecule reaction[13,14]

$$O^-+N_2O\rightarrow NO^-+NO,$$

$$\Delta H_0=-0.15\pm0.01 \text{ eV (Ref. 15).} \quad (1)$$

These studies show that reaction occurs through $O^-$ attack at both the terminal and central N atoms on $N_2O$. These results, when combined with the photoelectron spectra, imply that the reaction mechanism involves passing through two complexes corresponding to isomers (II) and (III), $NNO_2^-$ and $ONNO^-$.

Posey and Johnson found that at 532 and 355 nm, the only peak in the photoelectron spectrum of the $NNO_2^-$ isomer is from the photodetachment of $O^-$ atoms. Thus, at these wavelengths, photodissociation to $O^-+N_2O$ occurs rather than photodetachment of the parent $N_2O_2^-$ anion. More recently, Arnold and Neumark[16] have measured the photoelectron spectrum of this isomer at 266 and 213 nm. They found that at these higher photon energies, photodetachment of $N_2O_2^-$ does occur, populating several previously unknown electronic states of neutral $N_2O_2$. From this work alone, however, one cannot determine at what energy the observed $N_2O_2$ states lie relative to the various asymptotic channels

[a]Current address: Worlds, 510 Third St., Suite 530, San Francisco, CA 94107.
[b]Current address: Combustion Research Facility, Sandia National Laboratories, Livermore, CA 94551.

 0021-9606/96/104(13)/5026/14/$10.00 

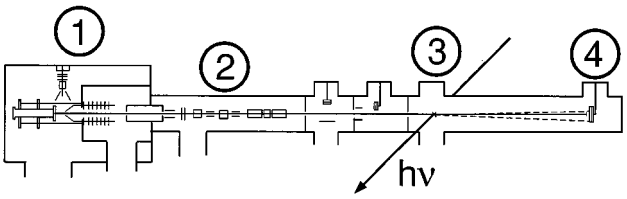


FIG. 1. The fast ion beam translational spectrometer: (1) ion source region; (2) mass selection and ion optics; (3) dissociation laser port; (4) time- and position-sensitive MCP detector. A more complete explanation of the apparatus, which was designed for photodissociation of neutral free radicals, can be found in Refs. 17 and 18.

($O+N_2O$, $N+NO_2$, $NO+NO$, etc.). One of the goals of this study is to answer this question by determining the dissociation energy of the $N_2O_2^-$ anion.

In this paper, we present recent work on the excited state spectroscopy and photodissociation dynamics of the $C_{2v}$ isomer (II), which will henceforth be referred to simply as $N_2O_2^-$. Using the technique of fast beam translational spectroscopy, we have measured the relative photodissociation cross section of $N_2O_2^-$ as a function of wavelength, and have performed more detailed dynamical measurements at selected wavelengths. We observe fragmentation to two channels, $O^-+N_2O$ and $NO^-+NO$, and have measured kinetic energy and angular distributions for both channels. These measurements yield bond dissociation energies and a wealth of information concerning the detailed photodissociation mechanism. The interpretation of our results is aided by *ab initio* calculations on the ground and excited states of $N_2O_2^-$ which are also reported here.

Section II of this paper describes the experimental apparatus used in this work, including a newly developed pulsed discharge negative ion source used in these and other experiments in our laboratory. Section III details the experimental data and the results of *ab initio* molecular orbital calculations. Section IV contains analysis of the results while Sec. V discusses the mechanism for dissociation and the potential energy surfaces that mediate this process.

## II. EXPERIMENT

### A. Fast beam translational spectrometer

The fast beam translational spectrometer used in these experiments was designed to study the photodissociation of neutral free radicals generated by photodetachment of a mass-selected anion beam, and has been described in detail elsewhere.[17,18] The anion photodissociation experiment described in this paper is somewhat simpler, as only one laser is required. The photodissociation of $O_4^-$ using a similar instrument has recently been reported by Continetti *et al.*[6] The experimental apparatus is shown in Fig. 1 and is briefly described as follows.

A pulsed supersonic expansion of 10% $N_2O$ in argon is either crossed with a 1 keV electron beam or subjected to a pulsed electric discharge to form an internally cold beam of $N_2O_2^-$. The pulsed discharge negative ion source developed in our laboratory was mentioned in a previous investigation,[19] and a full description will be given in Sec. II B. Anions formed in the source are accelerated to a laboratory energy of 8 keV, separated according to mass by a collinear beam modulation time-of-flight mass spectrometer,[20] axially compressed with a pulsed electric field, and slightly focused with an einzel lens. The dissociation laser, an excimer-pumped dye laser polarized perpendicular to the ion beam direction, is fired at the appropriate time to intersect only ions of mass 60. Photofragments which recoil out of the parent ion beam are detected with high efficiency using microchannel plate detectors located either 1 or 2 m from the photodissociation laser.

Two types of experiments are performed to characterize the photodissociation of $N_2O_2^-$. First, the total flux of photofragments is detected as a function of laser wavelength, mapping out the total dissociation cross section. In the second type of experiment the laser is operated at a fixed wavelength and the dissociation dynamics are investigated. For each dissociation event, the two photofragments are detected in coincidence. The position of both photofragments on the detector face and the time difference between their arrival are simultaneously recorded. From this experiment we obtain three important quantities that describe the photodissociation: product mass ratios, translational energy distributions, and angular distributions. The masses of the product fragments for each dissociation event can be determined by conservation of momentum in the center-of-mass frame. After correcting for the finite geometric acceptance of the detector, the center-of-mass recoil energy and recoil angle (with respect to the electric vector of the polarized laser) are analytically determined for each event.[18] The calibration of the detector by photodissociation of the Schumann–Runge bands in $O_2$ is discussed in detail elsewhere.[21] We record approximately one pair of fragments every 30 laser shots. A complete data set consisting of approximately 30 000 coincident events can be collected in 3–5 h. The energy resolution under the conditions in these studies is 25 meV.

The dynamics experiment requires that both fragments be detected. However, the front of the detector is biased at a high negative potential, such that only neutral fragments can be detected. Although the dissociation of $N_2O_2^-$ yields an ion and a neutral, the experimental conditions are such that the anion fragment is typically neutralized prior to reaching the detector. This fragment can be either photodetached by an additional photon from the dissociation laser, e.g.,

$$O^- + h\nu \rightarrow O + e^-, \quad NO^-(v=0) + h\nu \rightarrow NO + e^- \qquad (2)$$

or it can autodetach, since vibrationally excited $NO^-$ will lose an electron via[22]

$$NO^-(v>0) \rightarrow NO + e^-. \qquad (3)$$

(The electron affinity of NO is only 0.024 eV.) Hence, photodissociation of $N_2O_2^-$ followed by (2) or (3) results in two neutral fragments, enabling us to perform the coincidence experiment. We emphasize that even though only neutral particles are detected, this experiment nevertheless probes the

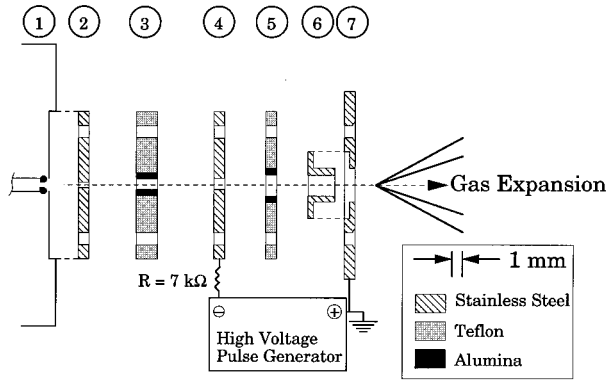


FIG. 2. The pulsed discharge negative ion source. Each component is described with its thickness ($T$) and gas channel diameter ($D$) given in mm for components 2–6. (1) Pulsed valve body; (2) pulsed valve faceplate [$T=2$, $D=0.6$]; (3) Teflon insulator with alumina insert along gas channel [$T=4$, $D=2$]; (4) cathode [$T=2$, $D=2$]; (5) Teflon/alumina insulator [$T=2$, $D=3$]; (6) Nozzle insert [$T=5$, $D=3$]; (7) Anode.

dynamics of ion dissociation, because the velocity vector of the nascent ionic fragment is not affected to any appreciable degree by the loss of an electron.

### B. Pulsed discharge negative ion source

One of the more successful pulsed negative ion sources developed in recent years is the design of Johnson *et al.*,[23] in which a pulsed molecular beam is crossed by a continuous beam of high energy (≈1000 eV) electrons. In this source, slow secondary electrons generated by ionization initiate ion-molecule chemistry which can be used to produce a wide variety of negative ions and negative ion clusters. A disadvantage of this source is that the secondary electrons are thermalized rapidly in the high number density of the pulsed free jet, so that only those processes which can be initiated by very low energy (1 eV) electrons can occur. Thus, the production of $F^-$ from $NF_3$ is very efficient, because this dissociative attachment process occurs for near zero energy electrons.[24] On the other hand, the production of $OH^-$ from $H_2O$ or $CH_3O^-$ from $CH_3OH$ does not work well in this source because dissociative attachment requires higher electron energies (>5 eV). An ion source in which higher energy processes can be efficiently driven is clearly desirable. To this end, we have developed a pulsed electric discharge negative ion source that is straightforward to build and use.

One can find examples of many pulsed supersonic expansion discharge sources in the literature for the production of neutral free radicals and cations. To our knowledge, the only published examples of negative ion production by these methods are given by Bondybey *et al.*[25] and Meiwes-Broer *et al.*[26] Our pulsed discharge negative ion source is similar in design to that used by Ohshima and Endo[27] for production of internally cold transient neutral species.

Figure 2 shows the details of the design. The faceplate (2) of the pulsed valve (1) is separated from the cathode (4) by a Teflon insulator (3). Discharge occurs through the channel of a second insulator (5), to the anode (7). For flexibility, nozzles (6) of various inner diameter, shape, and composition can be inserted into the anode to enhance or suppress clustering and/or cooling of the negative ions. Teflon screws secure the entire assembly to the pulsed valve faceplate. We have used the discharge source with either a piezoelectric pulsed valve of the type developed by Trickl[28] or a general valve solenoid valve.

The increasing channel diameter along the gas flow direction proved to be the crucial element in attaining intense internally cold negative ion beams. An advantage of this design is that ion formation occurs within the flow channel, *before* the expansion, maximizing the number of ion-neutral collisions that occur during the free jet expansion into the source chamber.

A pulse of −500 to −700 V is generated by a MOSFET switch[29] and applied to the cathode (3). The pulse is typically 15 μs in width, a fraction of the 150 μs gas pulse. The stability of the ion beam is increased if a very weak (<1 μA) electron beam intersects the gas flow as it emerges from the nozzle. This effect is most likely due to creation of positive ions which move against the gas flow towards the negatively charged cathode, acting as seeds to begin breakdown of the gas pulse. Ion stability and intensity is also increased when the discharge pulse comes very near the beginning of the gas pulse.

The duration of the discharge is 1–8 μs. The current through the discharge is followed by monitoring the voltage at the cathode both before and during breakdown of the gas. Typical discharge currents range from 5 to 30 mA depending on the composition of the gas mixture and the value of a ballast resistor (typically 7 kΩ) in series with the cathode. As the current through the discharge is increased, the voltage across the discharge increases only slightly, indicating that the discharge is essentially of the ''normal glow'' variety.[30]

Most gaseous precursor molecules are diluted to 1–10 % concentration with a carrier gas (e.g., Ar, Ne, or $O_2$) and expanded with a backing pressure of 2–8 atm. For liquid precursors the carrier gas is bubbled through the liquid. Substantial rearrangement of the precursor molecules is often observed. For example, a discharge of neon bubbled through methanol produces not only $CH_3O^-$, but also $C_2^-$, $C_2H^-$, and $C_2H_2^-$. Despite the high energy environment in which ions are formed, their internal degrees of freedom can still be effectively cooled in the supersonic expansion. Photofragment translational spectroscopy of predissociation from the $O_2$ Schumann–Runge band shows that an $O_2^-$ rotational temperature of ≈50 K can be attained.[31] For the case of $CH_3O^-$ produced in a discharge, photoelectron spectroscopy shows that 99% of these ions are in their vibrational ground state. These temperatures are as cold or colder than ions produced with the electron-gun source in our laboratory. In summary, we have found that the pulsed discharge negative ion source combines many of the strengths of other available sources with some significant new advantages. The source requires very little maintenance and is easily built at modest expense.

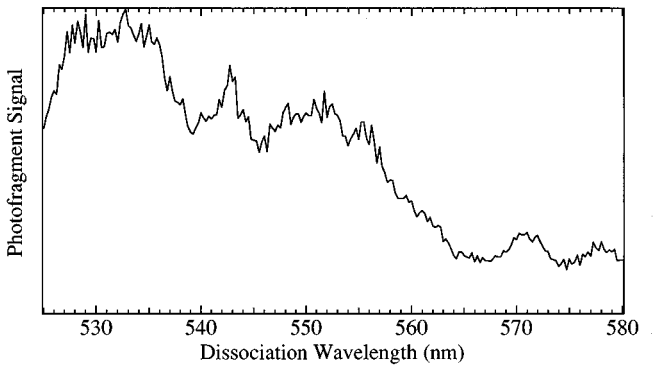


FIG. 3. Total photodissociation cross section spectrum of $N_2O_2^-$. Intensity is normalized to dissociation laser power. Laser step size is 0.25 nm.

## III. RESULTS

### A. Experimental data

Figure 3 shows the total dissociation cross section spectrum of $N_2O_2^-$ from 525–580 nm, normalized to dissociation laser power. The broad, partially resolved features in this spectrum are reproducible, although the finer structure ($<1$ nm) is not. The peak spacings range from $\approx$150 to 500 $cm^{-1}$, and are presumably due to excitation of multiple vibrational modes in the upper electronic state.

The main information we obtain about $N_2O_2^-$ photodissociation is derived from dissociation dynamics data acquired at three wavelengths: 570, 532, and 500 nm. Although wavelength resolved cross section data were not obtained below 525 nm, the cross section appears to be higher at 500 nm than at 532 nm. The first result from this dynamics data is the photofragment mass spectrum, shown in Fig. 4 for 532 nm dissociation. It is immediately seen that there are two product channels occurring at this wavelength:

$$N_2O_2^- + h\nu \rightarrow O^- + N_2O \quad \text{(channel 1)} \tag{4}$$

$$\rightarrow NO^- + NO \quad \text{(channel 2)} \tag{5}$$

with similar product mass spectra obtained at 500 and 570 nm.

For each channel, the joint translational energy and angular distribution is given by[18,32]

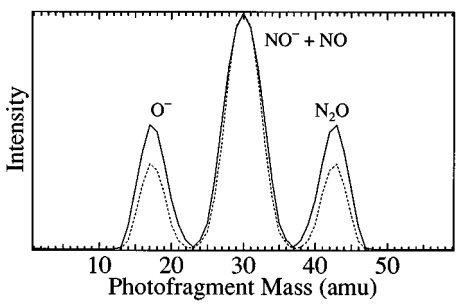


FIG. 4. Product mass spectrum at 532 nm as a function of laser fluence. The central peak corresponds to the channel (2) fragments, $NO^- + NO$. The other two peaks correspond to the channel (1) fragments, $O^- + N_2O$. Laser fluences are (—) 3.2 J/cm$^2$ and (---) 1.6 J/cm$^2$.

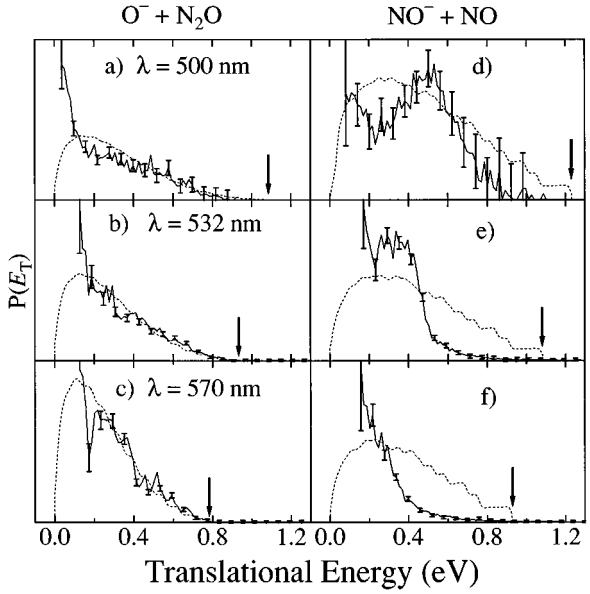


FIG. 5. Translational energy distributions $P(E_T)$ at three excitation energies (a)–(c) $O^- + N_2O$; (d)–(e) $NO^- + NO$. The solid lines connect the data points, which have error bars ($\pm 1\sigma$) on every fourth point. The dashed line is the prior distribution discussed in the text. The arrows denote the maximum energy available to translation for each photon energy/product channel combination.

$$P(E_T,\theta) \propto P(E_T)(1+\beta(E_T)P_2(\cos\theta)). \tag{6}$$

Here, $E_T$ is the translational energy release, $\theta$ is the angle between the photofragment recoil velocity vector and the laser polarization, and $\beta$ is the anisotropy parameter. Although $\beta$ can depend on the translational energy, no such dependence was observed here.

Figure 5 shows the translational energy release distribution $P(E_T)$ for both channels at each wavelength. Statistical error bars ($\pm 1\sigma$) are drawn for every fourth data point. All three translational energy distributions for channel 1 [Figs. 5(a)–5(c)] are maximal at the lowest translational energies we can detect, decreasing steadily towards higher $E_T$. For

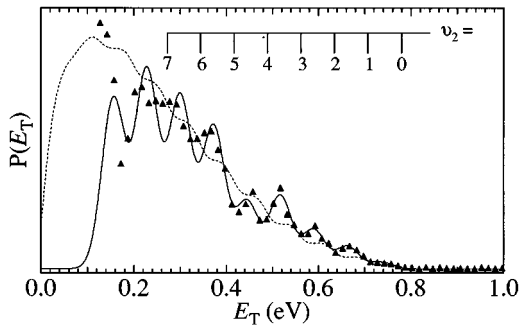


FIG. 6. Translational energy distribution for $O^- + N_2O$ at 570 nm. Triangles denote the experimental data, the solid line is the empirical fit [peak heights given by $\alpha_n$ of Eq. (10)] assuming bending excitation accounts for all $N_2O$ vibrational excitation. A vibrational comb is shown for the $\upsilon_2$ bending mode progression in the $N_2O$ fragment. The dashed line is the prior distribution given by Eq. (11).

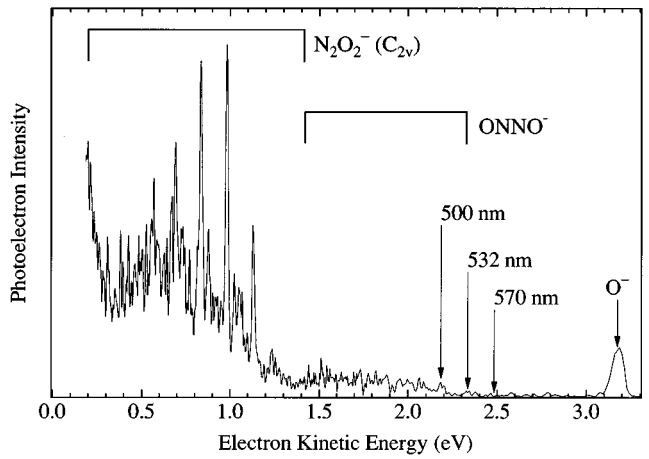


FIG. 7. 266 nm photoelectron spectrum of $N_2O_2^-$ using the pulsed discharge source. The sharp features at 1.13 eV and below are due to the $(C_{2v})N_2O_2$ neutral. The signal from 1.3–2.2 eV arises from an impurity of the $ONNO^-$ isomer (see text). The energies corresponding to the three dissociation wavelengths used in the present study are also shown.

the data at 570 nm in Fig. 5(c), which is replotted as Fig. 6, vibrational structure is apparent in the $P(E_T)$ distribution. The observed spacing corresponds to excitation of the bending mode ($\omega_2$=588 cm$^{-1}$) in the $N_2O$ fragment.[33] This structure is less evident as the photon energy is increased in Figs. 5(b) and 5(a). For the $NO^-$+NO channel in Figs. 5(d)–5(f), no vibrational structure is evident. Unlike channel (1), the most probable translational energy becomes larger as the photon energy is increased.

For the $NO^-$+NO channel, the angular distributions are isotropic ($\beta$=0) at all three wavelengths. For $O^-$+$N_2O$, the angular distributions are slightly anisotropic: $\beta$(570 nm)= $-0.15\pm0.2$, $\beta$(532 nm)=$-0.3\pm0.2$, and $\beta$(500 nm)=$-0.6$ $\pm0.3$. The anisotropy becomes more negative with increasing excitation energy. The uncertainty in the anisotropy parameter is a combination of a well-defined statistical error and an estimated systematic error which reflects the aberrations in our detector response for low translational energies. The values of the anisotropy parameter are related to both the symmetry and the lifetime of the excited anion states.

Because the data in this paper use the newly developed pulsed discharge source to produce $N_2O_2^-$, it is important to characterize the ions in this beam by comparing their photoelectron spectra, shown in Fig. 7, to that obtained by Arnold[16] using an electron gun source. We present this data (from a separate apparatus in our laboratory) because photoelectron spectroscopy is a sensitive probe of ion source conditions, as is evident from the work of Posey and Johnson[7] described earlier. The well-resolved vibrational structure seen in Fig. 7 at low electron kinetic energy (<1.2 eV) arises from bound neutral states of $N_2O_2(C_{2v})$. The weak electron signal from 1.3 to 2.2 eV is from photodetachment of isomer (III), $ONNO^-$, based on comparison with the spectra obtained when ions are produced from NO seeded in argon.[34] This isomer is not present under the gentler conditions of an electron gun ion source as used in Refs. 7 and 16.

The photon energies used to dissociate $N_2O_2^-$ are indicated by arrows in Fig. 7, demonstrating that direct photodetachment of the $C_{2v}$ isomer is not possible at these energies. However, the photoelectron spectrum in Fig. 7 does raise the possibility that the $NO^-$+NO product channel comes from photodissociation of the small amount of the $ONNO^-$ isomer produced in the pulsed discharge source. To examine this possibility we have performed the same photodissociation dynamics experiments described in this section using an electron gun ion source. The $NO^-$+NO photofragments are still observed in similar amounts as when $N_2O_2^-$ is produced in the pulsed discharge source, confirming that this is a primary product channel of ($C_{2v}$) $N_2O_2^-$ photodissociation. However, the $P(E_T)$ distributions also show that $N_2O_2^-$ produced by the electron gun ion source is not as efficiently cooled in the supersonic expansion; for example, no vibrational structure is apparent in the $O^-$+$N_2O$ $P(E_T)$ at 570 nm. For this reason we present data exclusively from the pulsed discharge source in this paper.

### B. *Ab initio* calculations

The product state information presented above is a direct result of the potential energy surfaces involved in the dissociation of $N_2O_2^-$. In order to gain more insight into the complicated electronic structure of the $N_2O_2^-$ system, we have performed *ab initio* molecular orbital calculations using the GUASSIAN92 package of programs.[35] In the recent work of Arnold and Neumark,[16] the ground state of $N_2O_2^-$ was assigned as $^2B_2$ with the orbital occupation ($\ldots 4b_2^2 2b_1^2 8a_1^2 1a_2^2 5b_2^1$), based on *ab initio* calculations [UHF (unrestricted Hartree–Fock) and MP2/6-31+G*) and comparison with the isoelectronic species $NO_3$ and $FCO_2$. We have extended these calculations to include the lowest excited states of each spatial symmetry within the $C_{2v}$ and $C_s$ point groups. The results of the $C_{2v}$ calculations are summarized in Table I.

Optimized geometries and vibrational frequencies were obtained at the UHF/6-31+G* level of theory. Five unique electronic states are found,[36] which, in order of increasing energy, are $^2B_2$, $^2A''$, $^2B_1$, $^2A_2$, and $^2A_1$ states. All of these configurations, with the exception of $^2A_2$, are bound along all vibrational coordinates. At the UHF level, the $^2A_2$ state is unbound along the $\nu_4$ ($NO_2$ asymmetric stretch) normal coordinate.

When electron correlation is taken into account at the MP2/6-31+G* level of theory, geometry optimizations reveal that the highest energy $^2A_1$ state has no stationary point within $C_{2v}$. In addition, the self-consistent field (SCF) wave function for the $^2A''(C_s)$ state is no longer convergent after a few steps in the (MP2 energy gradient) geometry optimization. For this reason we discuss no other calculations at $C_s$ geometries. At the MP2 level, therefore, the only electronic states which have stationary points along all coordinates are the ground state, $^2B_2$, and the first two excited states $^2B_1$, and $^2A_2$. Frequency calculations at these stationary points reveal that, just as at the UHF level, the first two states are bound along all coordinates, while the $^2A_2$ state has one

TABLE I. *Ab initio* results: Optimized geometries, energies, and vibrational frequencies (frequencies are in units of $cm^{-1}$).

| $\tilde{X}^2B_2$ | Energy[b] (Hartrees) | $\langle S^2\rangle$ | $T_e$ (eV) | $R_{NN}$ (Å) | $R_{NO}$ (Å) | ∠NNO° | $\omega_1$ ($A_1$) (NN str.) | $\omega_2$ ($A_1$) (NO str.) | $\omega_3$ ($A_1$) ($NO_2$ bend) | $\omega_4$ ($B_2$) ($NO_2$ a.s.) | $\omega_5$ ($B_2$) ($N_2O$ a.b.) | $\omega_6$ ($B_1$) (umbrella) |
|---|---|---|---|---|---|---|---|---|---|---|---|---|
| UHF | −258.494 495 | 0.920 | 0.0 | 1.253 | 1.253 | 119.2 | 1582 | 1086 | 692 | 1434 | 654 | 836 |
| MP2 | −259.165 961 | 0.926 | 0.0 | 1.270 | 1.253 | 120.3 | 1411 | 1241 | 679 | 1538 | 609 | 998 |
| QCISD | −259.190 341 | 1.022 | 0.0 | 1.267 | 1.296 | 120.0 | | | | | | |
| QCISD(T)[a] | −259.215 226 | 1.022 | 0.0 | | | | | | | | | |
| $\tilde{A}^2B_1$ | | | | | | | | | | | | |
| UHF | −258.438 789 | 0.778 | 1.52 | 1.352 | 1.220 | 120.1 | 1029 | 1404 | 735 | 1659 | 783 | 837 |
| MP2 | −259.124 816 | 0.797 | 1.12 | 1.354 | 1.274 | 120.6 | 990 | 1219 | 687 | 1389 | 800 | 713 |
| QCISD | −259.132 971 | 0.798 | 1.56 | 1.345 | 1.274 | 120.7 | | | | | | |
| QCISD(T)[a] | −259.161 024 | 0.798 | 1.47 | | | | | | | | | |
| $\tilde{B}^2A_2$ | | | | | | | | | | | | |
| UHF | −258.407 553 | 1.404 | 2.36 | 1.255 | 1.320 | 126.6 | 1364 | 1018 | 707 | 1668*i* | 685 | 470 |
| MP2 | −259.066 859 | 1.161 | 2.70 | 1.131 | 1.479 | 130.3 | 2177 | 613 | 472 | 1559*i* | 666 | 716 |
| QCISD | −259.101 678 | 1.306 | 2.41 | 1.194 | 1.417 | 128.7 | | | | | | |
| QCISD(T)[a] | −259.133 796 | 1.306 | 2.24 | | | | | | | | | |
| $\tilde{C}^2A_1$ | | | | | | | | | | | | |
| UHF | −258.325 524 | 0.882 | 4.60 | 1.205 | 1.347 | 122.3 | 1113 | 884 | 659 | 2264 | 655 | 689 |

[a]QCISD(T) energies are evaluated at the QCISD/6-31+G* geometry.
[b]All calculations use the standard 6-31+G* basis set.

imaginary frequency. In order to treat electron correlation more rigorously, geometries for the lowest three states were further optimized at the QCISD/6-31+G* level of theory, with a single point QCISD(T) calculation at this geometry. No vibrational frequencies were calculated at this level of theory. Finally, vertical excitation energies from the ground state are also shown at each level of theory in Table II.

The results in Table I show marked differences in the structures of the $\tilde{X}$, $\tilde{A}$, and $\tilde{B}$ states. The ground state structure ($R_{NN}$=1.27 Å, $R_{NO}$=1.30 Å) is best described as an N–N double bond [$R_{NN}$=1.254 Å in $(CH_3)_2N_2$ (Ref. 37)] and an N–O distance intermediate between single ($R_{NO}$=1.398 Å in $CH_3O$–NO) and double ($R_{NO}$=1.212 Å in HNO) bond character. In the $\tilde{A}(^2B_1)$ state, the N–N bond length increases to $R_{NN}$=1.35 Å, indicating that it too is now intermediate between single ($R_{NN}$=1.447 Å in $N_2H_4$) and double bond character. The N–O bond length is very similar to that of the ground state, differing by only 0.02 Å. In both the *X* and *A* states the geometries are not strongly dependent on the level of theory. In the $\tilde{B}(^2A_2)$ state, the bond lengths and bond angles change quite drastically when electron correlation is included with the MP2 or QCISD methods. The QCISD optimized geometry ($R_{NN}$=1.19 Å, $R_{NO}$=1.42 Å) is characterized by an N–N bond intermediate between double and triple ($R_{NN}$=1.094 Å in $N_2$), and an N–O bond significantly longer than a typical single bond. It is also useful to compare these bond lengths with that of the photofragments observed in this study. In $N_2O$, $R_{NN}$=1.128 Å, $R_{NO}$=1.184 Å,[33] while for NO and $NO^-$ the respective bond lengths are $R_{NO}$=1.151 Å, and 1.25 Å.[22]

To determine the degree of confidence that one can place in the *ab initio* results, one can examine both spin contamination and the sensitivity of the calculated geometries and frequencies to the level of calculation. The unrestricted Hartree–Fock wave functions of all states suffer from some degree of spin contamination by states of higher multiplicity. As shown in Table I, spin contamination ($\langle S^2\rangle$=0.75 for a pure doublet state) is quite large for the $\tilde{B}(^2A_2)$ state, small for the $\tilde{A}(^2B_1)$ state, and somewhere in between for the ground state. In terms of structural parameters, for the ground state the largest change in bond length (0.04 Å) and bond angle (1°) is relatively modest for the different treatments. In the $\tilde{A}(^2B_1)$ state the only significant change is in $R_{NO}$, which increases by 0.05 Å between UHF and the two correlated methods, the latter two calculations yielding essentially identical geometries. For the $\tilde{B}(^2A_2)$ state the results are less satisfying: the bond lengths and angles change by significant amounts (0.06–0.12 Å; 2–4°) at the three levels of theory. The percent change in each vibrational frequency ($\omega_{UHF}/\omega_{MP2}$) for the $\tilde{X}$ and $\tilde{A}$ states is at most 19%, while in the *B* state four of the six frequencies change by 50–60 %. Therefore one must treat the *ab initio* results with

TABLE II. Vertical excitation energies (energies in eV).

| | UHF | MP2 | MP4SDTQ | QCISD | QCISD(T) |
|---|---|---|---|---|---|
| $\tilde{C}(^2A_1)$ | 4.90 | 3.90 | 4.11 | 3.78 | 3.52 |
| $\tilde{B}(^2A_2)$ | 3.07 | 3.86 | 4.08 | 3.30 | 3.24 |
| $\tilde{A}(^2B_1)$ | 1.72 | 1.46 | 1.40 | 1.67 | 1.59 |
| $\tilde{X}(^2B_2)$ | 0.0 | 0.0 | 0.0 | 0.0 | 0.0 |

TABLE III. G1 and G2 *ab initio* energies and heats of reaction.

| Species | $E_0$ [$G1$] (hartrees) | $E_0$ [$G2$] (hartrees) |
|---|---|---|
| $\tilde{X}(^2B_2)N_2O_2^-$ | −259.525 136 | −259.525 952 |
| $\tilde{X}(^2A_g)$ trans-ONNO$^-$ [a] | −259.527 065 | −259.527 948 |
| $\tilde{X}(^1\Sigma_g^+)N_2O$ | −184.437 103 | −184.437 117 |
| $\tilde{X}(^2\Pi_g)$NO[b] | −129.739 12 | −129.739 95 |
| $\tilde{X}(^3\Sigma_g^-)$NO$^-$ [b] | −129.736 89 | −129.737 52 |
| $(^2P_u)O^-$ [b] | −75.033 85 | −75.033 41 |
| Reaction | $\Delta H_0$ [$G1$] (eV) | $\Delta H_0$ [$G2$] (eV) |
| $N_2O_2^-(C_{2v})\rightarrow O^-+N_2O$ | 1.47 | 1.51 |
| $N_2O_2^-(C_{2v})\rightarrow NO^-+NO$ | 1.34 | 1.32 |
| $O^-+N_2O\rightarrow NO^-+NO$ | −0.14 | −0.19 |
| $N_2O_2^-(C_{2v})\rightarrow$trans-ONNO$^-(C_{2h})$ | −0.05 | −0.05 |

[a]The *cis* ($C_{2v}$) isomer lies 0.1 eV higher at the MP2/6-31+G* level of theory.
[b]Energies taken from Ref. 39.

some caution, particularly for the $\tilde{B}$ state, in which all three criteria show signs that the single-configuration picture may not be sufficient for a quantitative description.

For comparison with the thermodynamic information obtained from the data in Sec. IV, we have also performed Gaussian-1 (G1) and Gaussian-2 (G2) calculations[38,39] giving the total electronic energies (including zero-point energies) of $\tilde{X}(^2B_2)$ $N_2O_2^-$, $\tilde{X}(^2A_g)$ *trans*-ONNO$^-$, and $\tilde{X}(^1\Sigma_g^+)$ $N_2O$. These calculations are summarized in Table III. The ONNO$^-$ configuration is included because it is also strongly bound and has been implicated as a reaction intermediate in reaction (1). The G1 and G2 procedures, due to Pople and co-workers, are quite successful in predicting dissociation energies to within a target accuracy of ±0.1 eV (2 kcal/mol) for a wide range of neutral and ionic species. Within the accuracy of these calculations, $N_2O_2^-$ ($C_{2v}$) and ONNO$^-$ ($C_{2h}$) are essentially thermoneutral. This differs from the lower-level calculation in Ref. 8, which predicts the $C_{2v}$ isomer to be more stable by 4.4 kcal/mol.

## IV. ANALYSIS

### A. Product branching ratio

In Fig. 4, the ratio between the peak areas for channel 1:channel 2 at the higher laser fluence is about 1:1. However, the extraction of quantitative branching ratios from this data is more complicated in the case of $N_2O_2^-$ photodissociation than in our previous studies of free radical photodissociation. As mentioned in Sec. II, only neutral fragments can be detected with our time- and position-sensitive detector. Although both product channels result from single photon dissociation, *detection* of $O^-+N_2O$ requires a second photon (to detach the $O^-$ fragment), while $NO^-$ ($v>0$)+NO detection does not require another photon due to autodetachment of the $NO^-$ fragment. The channel 1:channel 2 peak area ratio increases with laser fluence over the entire range available to us, indicating that the two photon process producing $O+N_2O$ is not yet saturated. Therefore the branching ratio stated above should be taken as a lower bound to the true channel 1:channel 2 branching ratio at 532 nm, because not all of the $O^-$ is photodetached even at the highest laser fluence. Thus, while quantitative branching ratios cannot be obtained, it is clear that $O^-+N_2O$ is the major product channel.

### B. Dissociation energies and product energy distributions

From the translational energy distributions $P(E_T)$ in Fig. 5, we can extract both thermodynamic data and information on product state energy disposal resulting from $N_2O_2^-$ photodissociation. By conservation of energy we may write

$$h\nu = D_0(N_2O_2^-\rightarrow O^-+N_2O)+E_T E_{\text{int}}(N_2O), \tag{7}$$

$$h\nu = D_0(N_2O_2^-\rightarrow NO^-+NO)+E_T+E_{\text{int}}(NO) + E_{\text{int}}(NO^-), \tag{8}$$

where $h\nu$ is the photon energy, $D_0$ is the dissociation energy for the specified channel, $E_T$ is the energy in product translation, and $E_{\text{int}}$ is the rotational, vibrational, and electronic energy of the molecular fragments. We assume in Eqs. (7) and (8) that the supersonically cooled $N_2O_2^-$ parent ion contains negligible internal energy. If for some translational energy $E_T$ it can be ascertained that $E_{\text{int}}=0$, the dissociation energy in the aforementioned equations can be deduced. Given these thermodynamic quantities, the total internal energy of the fragments corresponding to each energy $E_T$ is determined, and in some cases this energy can be further delineated among rotational, vibrational, and electronic degrees of freedom.

The most detailed information can be obtained from Fig. 6, showing an expanded picture of the $P(E_T)$ at 570 nm for $O^-+N_2O$. This distribution shows a series of peaks with spacings close to that of the $\upsilon_2$ bending mode of the $N_2O$ product. The resolved vibrational structure is significant, as this spectrum offers substantially more information than the qualitatively similar spectrum shown in Fig. 5(a). At 570 nm, no signal is observed for $E_T > 0.78 \pm 0.03$ eV $\equiv E_T^{\max}$. Because the disappearance of signal at $E_T^{\max}$ is quite abrupt, we assign it to the translational energy corresponding to ground state fragments, i.e., $O^-$ ($^2P_{3/2}$)+$N_2O$ ($v=0$, $J=0$). We therefore obtain

$$D_0(N_2O_2^- \rightarrow O^- + N_2O) = h\nu - E_T^{max} = 1.40 \pm 0.03 \text{ eV}, \quad (9)$$

where $h\nu = 2.175$ eV. This value agrees to within 0.1 eV of the calculated Gaussian-2 value given in Table III (1.51 eV). From the 0 K heats of formation of $O^-$ (1.10 eV) and $N_2O$ (0.88 eV),[40] we obtain the heat of formation of $N_2O_2^-$: $\Delta H_{f,0}^0 = 0.58 \pm 0.04$ eV. From $\Delta H_0$ for reaction (1) we find that $D_0(N_2O_2^- \rightarrow NO^- + NO) = 1.25 \pm 0.04$ eV. These values of $D_0$ yield the maximum allowed values for $E_T$ at each dissociation wavelength, which are shown by the arrows in Fig. 5.

Based on the bond dissociation energy in Eq. (9), the thresholds for $O^- + N_2O$ ($v_2 = n$) are indicated by the comb in Fig. 6. The correspondence with the experimental peak spacings is quite good for $n < 6$. All the experimental peaks are offset towards lower translational energy than the thresholds for each vibrational state. This offset is presumably due to rotational excitation of each $N_2O$ vibrational level. Hence, from this vibrationally resolved $P(E_T)$ distribution we would like to determine the vibrational and rotational energy distribution of the $N_2O$ fragment.

The simplest way to extract such information is to assume that all of the $N_2O$ excitation is in the $v_2$ mode. We then construct an empirical model of the $P(E_T)$ distribution using a set of Gaussian peaks separated by the known vibrational spacings (588 $cm^{-1}$) of the $v_2$ mode. A Gaussian functional form is chosen to model the rotational distribution purely on the basis of mathematical convenience. The model distribution $F(E_T)$ is given by $n'+1$ Gaussians such that

$$F(E_T) = \sum_{n=0}^{n'} \alpha_n f_n(E_T),$$

$$f_n(E_T) = \exp\left[ -\frac{1}{2} \left( \frac{E_T - (h\nu - D_0 - n\omega_2 - \Delta)}{\Gamma/2.345} \right)^2 \right]. \quad (10)$$

Here $n$ labels the number of $N_2O$ bending quanta, $\Gamma$ is the full width at half maximum (FWHM) of the combined rotational envelope and instrumental resolution, and $\Delta$ is the energy difference between the maximum possible $E_T$ for each $n$ [$E_T^{max}(n) = h\nu - D_0 - n\omega_2$] and the center of the $n$th Gaussian. Each $f_n(E_T)$ is truncated for $E_T > E_T^{max}(n)$, the limit corresponding to $N_2O$ ($J = 0$). The coefficients $\alpha_n$ give the $v_2$ product state vibrational distribution. The solid line in Fig. 6 shows the best fit to the 570 nm $P(E_T)$ from a nonlinear least squares fitting procedure, with parameters $\Delta = 0.045$ eV, $\Gamma = 0.058$ eV. Note that the same values of $\Delta$ and $\Gamma$ were used for all vibrational states.

The fit is excellent for $E_T < 0.35$ eV. The less than satisfactory agreement below this energy may reflect excitation of other $N_2O$ vibrational modes. In fact, it is difficult to tell from the 570 nm $P(E_T)$ if excitation in the stretching modes is occurring at low $E_T$, because the frequencies of the $N_2O$ $v_1$ and $v_3$ modes are nearly integer multiples of the $v_2$ frequency: $\omega_1 = 3.8\omega_2$ and $\omega_3 = 2.2\omega_2$. The possibility that there is excitation in all the $N_2O$ modes has important implications for the dissociation mechanism and is discussed in more detail in Sec. V.

The vibrational structure in the experimental distributions is not as well resolved at 532 nm as at 570 nm, and at 500 nm it is difficult to pick out any vibrational structure. This blurring can again be attributed to either increasing product rotational energy, or a breakdown in the assumption that all vibrational excitation of $N_2O$ occurs as bending motion. In the absence of resolved structure, we do not attempt to fit the $P(E_t)$ distributions at the higher excitation energies with Eq. (10).

We next consider the translational energy release distributions for channel (2). In contrast to channel (1), for which all the $P(E_T)$ curves peak at the low energy cutoff of our instrument, in channel (2) it is clear that with increasing photon energy the peak in the translational energy distribution shifts to higher energy. Furthermore, each increase of photon energy, which corresponds to a 150 meV increment, shifts the peak of the $P(E_T)$ distributions to higher energy by approximately 150 meV. In other words, even though the 570 nm $P(E_T)$ distribution peaks at or below our low-energy cutoff, with little of the available energy going into fragment translation, the extra energy available at 532 and 500 nm is, on average, channeled into translational energy.

The $P(E_T)$ distributions for channel (2) [Figs. 5(d)–(f)] can be fit in the same manner as those for channel (1). These fits are underdetermined due to the lack of vibrational structure and the fact that there are two molecular fragments, NO and $NO^-$, which may both be rovibrationally excited. Even so, the density of vibrational product states is smaller for this case of two diatomics than for the products $O^- + N_2O$. The absence of resolved vibrational structure and the observation that the $P(E_T)$ distributions fall to zero well below $E_T^{max}$ implies that both fragments have considerable vibrational and rotational excitation. At all three wavelengths there is very little probability of finding both diatomic fragments in their $v = 0$ vibrational states. We will show in Sec. V that a high degree of $NO^-$ vibrational excitation is consistent with the photoelectron spectroscopy results of Posey and Johnson,[7] in which no evidence for the $NO^- + NO$ channel was evident.

## V. DISCUSSION

### A. Dissociation mechanism: $N_2O_2^- + h\nu \rightarrow O^- + N_2O$

We first consider the nature of the excited electronic state of $N_2O_2^-$ accessed in these experiments followed by a discussion of how this state dissociates to $O^- + N_2O$ products. To assign the initial electronic excitation we compare our experimental results with the *ab initio* calculations summarized in Tables I and II. The transition to the first excited state, $\tilde{A}(^2B_1) \leftarrow \tilde{X}(^2B_2)$, with a calculated $T_e = 1.47$ eV, is not electric dipole allowed. The lowest allowed transition, $\tilde{B}(^2A_2) \leftarrow \tilde{X}(^2B_2)$, has a calculated energy of $T_e = 2.24$ eV ($\lambda = 553$ nm), and a vertical excitation energy of 3.24 eV ($\lambda = 382$ nm). The photodissociation cross section in Fig. 3 starts near the predicted $T_e$ for this transition, and rises steadily towards the blue as would be expected when the vertical excitation energy is considerably larger than $T_e$. Furthermore, we measure a negative photofragment anisotropy

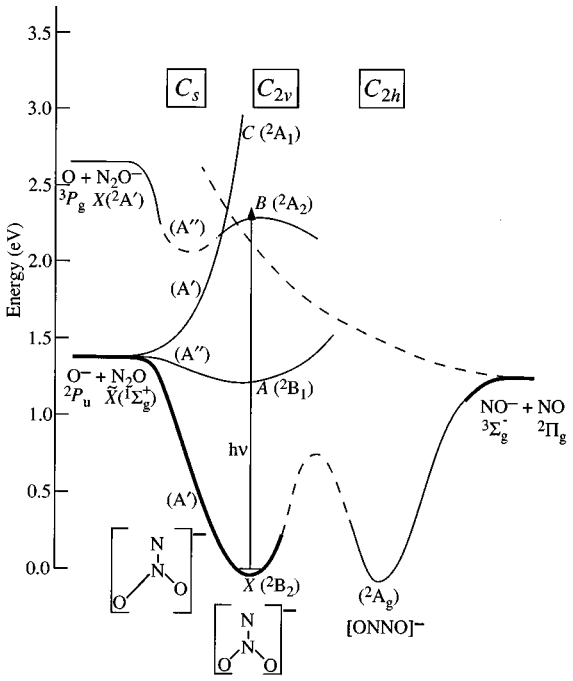


FIG. 8. One-dimensional projections of potential energy surfaces of the $N_2O_2^-$ system. The nuclear coordinate is approximately represented by the structures shown along the bottom of the diagram. Below the label for each symmetry group ($C_s$, $C_{2v}$, $C_{2h}$) are listed the electronic states of that symmetry, showing the correlation of electronic states. Energy differences between the $X(^2B_2)$ minimum and the two asymptotes are those derived from this experiment (thick lines). Thin lines are based on the *ab initio* results and molecular orbital correlations. Surfaces depicted by dashed lines are plausible guesses for which no calculations have been successful. According to our calculations (Table I), the $B(^2A_2)$ state does not have a local minimum in $C_{2v}$ symmetry, but this may be a symmetry-breaking artifact (see text).

parameter, $\beta$, indicating that the initial electronic excitation is a perpendicular transition. The $\tilde{B}(^2A_2) \leftarrow \tilde{X}(^2B_2)$ transition has the required perpendicular character, involving the promotion of an electron from the doubly occupied out-of-plane $1a_2$ orbital to the singly occupied in-plane $5b_2$ orbital. Based on these considerations, we assign the electronic excitation of the $N_2O_2^-$ ion in our experiment to the first optically allowed transition $\tilde{B}(^2A_2) \leftarrow \tilde{X}(^2B_2)$.

In order to consider the dissociation dynamics subsequent to electronic excitation, it is important to understand how the electronic states of $N_2O_2^-$ correlate to product channels. Figure 8 represents the adiabatic picture of the relevant surfaces, where the lowest states of each symmetry are correlated to asymptotic states to determine the evolution of the electronic wavefunctions. As dissociation begins towards the $O^- + N_2O$ asymptote, the extension of the N–O bond lowers the ion's symmetry from $C_{2v}$ to $C_s$, such that the in-plane orbitals ($a_1$ and $b_2$) become $a'$ while the out-of-plane orbitals ($a_2$ and $b_1$) correlate to $a''$. On the other hand, if one approaches from the asymptotic region, $N_2O_2^-$ is formed by combining $O^-(^2P_u)$ with $N_2O$ ($^1\Sigma_g^+$), resulting in three electronic states of $C_s$ symmetry: $A'$, $A'$, and $A''$. By adiabatically correlating the lowest states of each symmetry, the $\tilde{X}(^2B_2)$ ground state becomes $^2A'$, while the $\tilde{A}(^2B_1)$ excited state matches with $A''$. The third state, $\tilde{B}(^2A_2)$, *cannot* correlate with the remaining $A'$ state, and must instead be matched with an $A''$ state that adiabatically leads to $O(^3P_g) + N_2O^-(^2A')$. These products are not energetically accessible at the photon energies used in the present study. The remaining $A'$ state arising from $O^-(^2P_u)$ with $N_2O(^1\Sigma_g^+)$ most likely correlates with the unbound $\tilde{C}(^2A_1)$ state, although it is possible that a lower-lying $^2B_2$ state exists.

The key feature of Fig. 8 is that the $\tilde{B}(^2A_2)$ state, which we assign as the initial excited state in our experiment, does not correlate to ground state $O^- + N_2O$ products. A nonadiabatic transition to another electronic surface is required in the dissociation mechanism. The question remains as to whether dissociation occurs on an excited state surface, such as the repulsive $\tilde{C}(^2A_1)$ state, or if internal conversion to the ground state occurs prior to dissociation. The translational energy distributions $P(E_T)$ in Fig. 5 can, in principle, help distinguish between these possible mechanisms.

The excited state mechanism appears reasonable at first glance. Given that $N_2O$ is linear, whereas the N–N–O moiety in $N_2O_2^-$ is strongly bent, one would expect significant excitation in the $N_2O$ bend from excited state dissociation on a repulsive surface, which is consistent with the vibrational structure seen in the translational energy distribution at 570 nm. This mechanism would also result in relatively little $N_2O$ rotational excitation, since the departing $O^-$ ion cannot apply much torque to the $N_2O$ fragment; this is again consistent with the observation of resolved vibrational structure in the $P(E_T)$ distribution, at least at 570 nm.

However, photodissociation studies of many small molecules have shown that when dissociation occurs on a repulsive potential energy surface, the translational energy distribution peaks well away from $E_T = 0$. In contrast, all three experimental distributions for this channel peak near zero translational energy, and their overall shape is relatively independent of photon energy [compared to channel (2), for example]. This trend is what one might expect if the dissociation mechanism were internal conversion to the ground state, followed by statistical decomposition without an exit barrier. The absence of a barrier is certainly reasonable for bond fission yielding an ion/neutral fragment pair, which will be governed by an attractive potential proportional to $-1/r^4$. It is useful for the moment to bypass the first step in this mechanism, internal conversion to the ground state, to determine if the observed translational energy distributions are consistent with statistical theory.

#### 1. Prior distributions

The most straightforward comparison one can draw is with the prior translational energy distribution[41] for the photofragments. This model is expected to be most appropriate for a potential without an exit barrier, in which the transition state lies far enough in the exit channel that the nuclear configuration is essentially that of the products. One can then use the rotational constants and vibrational frequencies of $N_2O$ in computing the prior distribution.

In order to compute the prior translational energy distribution, the vibrations are treated as discrete quantum states, while to good approximation the translational and product

rotational degrees of freedom can be treated as continuous distributions. Based on the treatment by Levine,[41] one can show that the prior translational energy distribution $P^0(E_T)$ for the $O^-+N_2O$ channel is given by

$$P^0(E_T)=C^0\sum_{v_1,v_2,v_3=0}^{E_v<E_{\text{avail}}-E_T} g(v_1,v_2,v_3)(E_T)^{1/2}. \tag{11}$$

Here $E_{\text{av}}=h\nu-D_0$ is the total energy available to the products and $g(v_1,v_2,v_3)$ is the degeneracy of the specified $N_2O$ vibrational level; at each $E_T$, the sum is over all energetically allowed $N_2O$ vibrational levels.

The prior distributions resulting from Eq. (11), convoluted with a 0.025 eV FWHM Gaussian instrument resolution function, are superimposed on the experimental distributions in Figs. 5(a)–5(c) and Fig. 6. The prior distributions peak near $E_T=0.1$ eV (our experimental cutoff), decreasing towards higher $E_T$. Overall, the agreement between the prior and experimental distributions is quite good, except at the very lowest values of $E_T$ where the error bars on the experimental $P(E_T)$ are large. The prior distributions match the general shape of the experimental distributions, and at each wavelength both distributions drop to zero at approximately the same value of $E_T$. Moreover, there is observable vibrational structure in the 570 nm prior distribution which becomes less prominent at lower wavelengths, in agreement with the experimentally observed trend.

In Fig. 6 one can make a more detailed comparison between the prior and experimental distributions at 570 nm. Like the experimental data, the prior distribution contains periodic structure on an interval that matches the $v_2$ bending mode of $N_2O$. Even though all three vibrational modes are excited, the $v_2$ mode dominates the statistical distribution because it is $(n+1)$-fold degenerate when $n$ bending quanta are populated. Because of this effect, combined with the difficulty (see Sec. IV) in distinguishing $v_2$ excitation from excitation in the $v_1$ and $v_3$ modes of $N_2O$, it is possible for even a statistical distribution of product states to support a 588 $cm^{-1}$ (i.e., $\omega_2$) vibrational spacing in the translational energy distribution. We make this point because the experimental data at 570 nm may also be modeled quite convincingly by Eq. (10) (solid line in Fig. 6) to represent excitation of pure $N_2O$ bending motion, an interpretation that is irreconcilable with a statistical dissociation mechanism.

However, a closer comparison shows that structure in the prior distribution is broader than the experimental rotational envelope at 570 nm, particularly at high $E_T$. This broadening arises because for each $N_2O$ vibrational level $(v_1,v_2,v_3)$, the corresponding term in the summation of Eq. (11) begins abruptly at $E_T=E_{\text{av}}-E_v$. For this reason the thresholds in the prior distribution line up well with the vibrational comb in Fig. 6. In addition, for each vibrational state the prior distribution extends all the way to $E_T=0$, i.e., the maximum $E_j$ allowed by energy conservation. This yields very broad rotational energy distributions for low vibrational states of $N_2O$, with narrower distributions only for the highest vibrational states. In contrast, the fitting of the experimental data to Eq. (10) indicates that the rotational envelope for each state is about the same, and is considerably narrower than that resulting from the prior distribution.

This discrepancy may simply indicate that the rotational distribution reflects the dissociation dynamics on the ground state surface, and that the constraints on $N_2O$ rotation imposed by energy and angular momentum conservation alone are physically unreasonable. While there is some rotational excitation of the $N_2O_2^-$ in the ion beam, if we assume that the total angular momentum $J\cong 0$, then the $N_2O$ rotational angular momentum $j$ is approximately equal in magnitude to $l$, the orbital angular momentum of the separating fragments. Consider, for example, the $N_2O$ $(v_2=4)$ level, for which the maximum $E_T$ is 0.48 eV at 570 nm. The value of $j_{\max}=l_{\max}$ determined by energy conservation alone is $96\hbar$, while $l_{\max}$ determined by considering the maximum $l$ at which the translational energy is greater than the centrifugal exit barrier (assuming the appropriate $-1/r^4$ long range potential) is only slightly smaller, $93\hbar$. The corresponding impact parameters, given by $\mu v b_{\max}=l_{\max}$, are 1.84 and 1.79 Å, respectively, both of which are considerably greater than the radius of the $N_2O$ molecule, 1.156 Å. Given that the $O^-$ is originally bound to the central N atom of the $N_2O$ fragment, these values appear to be unreasonably large even if there is substantial large amplitude vibrational motion on the ground state surface prior to dissociation. In this context it is not altogether surprising that the experimental rotational distributions are narrower than those predicted by statistical models.

Based on the reasonable overall agreement between the experimental results and prior distributions, we believe that the $O^-+N_2O$ channel results from decay on the ground state surface rather than dissociation on a repulsive excited state. While the latter mechanism certainly cannot be ruled out, it would be unusual for the translational energy distribution from such a process to be so similar to that predicted by a simple statistical model.

### *2. Angular distributions and RRKM lifetimes*

The angular distributions and their dependence on excitation energy provide further insight into the dissociation dynamics. Recall that the angular distribution is essentially isotropic at 570 nm and that the anisotropy increases with energy. This indicates that the lifetime of the $N_2O_2^-$ complex is several rotational periods at 570 nm, whereas at 500 nm the lifetime is shorter, presumably more on the order of the characteristic rotational period of the complex. If we assume a rotational temperature of 60 K and treat the complex as an oblate symmetric top with rotational constants determined from the ground state geometry, the average value of rotational quantum number $J$ is 11. The corresponding classical rotational period about the $c$-axis of the complex (i.e., perpendicular to the plane) is 6.3 ps.

It is of interest to compare the rotational period to the Rice–Ramsperger–Kassel–Marcus (RRKM) lifetime of $N_2O_2^-$ in its ground electronic state. The RRKM dissociation rate $k(E)$ is given by

$$k(E)=N^{\ddagger}(E^{\ddagger})/h\rho(E). \tag{12}$$

Here $N^{\ddagger}(E^{\ddagger})$ is the number of accessible states at the transition state and $\rho(E)$ is the density of $N_2O_2^-$ states at total energy $E$, both of which can be calculated from the Whitten–Rabinovitch expressions[42] if the vibrational frequencies of the transition state and reactant are known. Because no barrier to dissociation is expected, we choose a loose transition state with four vibrational frequencies set equal to the $N_2O$ frequencies and one low frequency vibration corresponding to the in-plane $O–N_2O$ bend (the $O^-–N_2O$ asymmetric stretch is taken to be the reaction coordinate). The calculated vibrational frequencies at the MP2 level are used to calculate $\rho(E)$ for $N_2O_2^-$. If the $O–N_2O$ bend frequency in the transition state is assumed to be 50 $cm^{-1}$, the resulting lifetime of the complex at 570 nm is 0.13 ps, considerably shorter than the rotational period. We note that the preexponential $A$ factor calculated with these transition state and reactant frequencies is only $2\times10^{14}$ $sec^{-1}$ (at $T=300$ K). This value is somewhat low for dissociation without a barrier; more typical values are $10^{16}$ $sec^{-1}$.[43] Thus our assumed transition state is, if anything, too ''tight.'' It might be more realistic to use a lower bend frequency or an internal rotor to model the relative motion of the $O^-$ and $N_2O$ fragments at the transition state, in which case the dissociation lifetime would be even shorter.

The large discrepancy between the apparent dissociation lifetime implied by the angular distributions and the RRKM lifetime suggests that dissociation on the ground state potential energy surface is not the rate-limiting step. A possible explanation is that internal conversion from the initially excited $\tilde{B}(^2A_2)$ state to the ground state occurs on a time scale of several picoseconds and is therefore rate limiting. We would then attribute the decrease in lifetime with increasing excitation energy to an increased internal conversion rate arising from more highly excited vibrational levels of the $B(^2A_2)$ state.

### B. Dissociation mechanism: $N_2O_2^- + h\nu \rightarrow NO^- + NO$

The description of product channel (2), which yields $NO^- + NO$, requires a discussion of several of the same issues raised in considering channel (1). However, channel (2) is clearly more complex, as it involves rearrangement and elimination, rather than the simple bond fission process of channel (1). A key issue in the mechanism of channel (2) is the role of the $ONNO^-$ isomer. Posey and Johnson[7] showed that this isomer (which they denote $NO^-NO$) is a stable species on the global potential energy surface of the negative ion. There is no experimental evidence for the exact energy of this isomer relative to the $N_2O_2^-(C_{2v})$ well. The only previously published calculation, by Hiraoka *et al.* at the ROHF/6-31+G level, finds the $C_{2v}$ structure more stable than trans-$ONNO^-$ ($C_{2h}$) by 4.4 kcal/mol.[8] Our G1 and G2 calculations described in Sec. III B show that at this more accurate level of theory the two isomers are essentially isoenergetic, with the trans-$ONNO^-$ isomer more stable by only 0.05 eV. The depth of this well on the potential energy surface depicted in Fig. 8 is based on the G-2 calculations. Although the photoelectron spectrum offers no clues as to the relative thermodynamics of these two isomers, we can be certain that the anion potential energy surface has a well in an $ONNO^-$ configuration.

Based on the discussion of channel (1), the first mechanism which must be considered, aside from the initial electronic excitation, is that the dynamics for channel (2) occur entirely on the global ground state potential energy surface for the $O^- + N_2O \rightarrow NO^- + NO$ reaction. Specifically, electronic excitation would be followed by internal conversion to the $N_2O_2^-$ ground electronic state, after which isomerization to $ONNO^-$ and bond fission to $NO^- + NO$ occur. The result of this mechanism would be experimental $P(E_T)$ distributions which, like those for channel (1), should reflect a largely statistical decomposition mechanism for a process with no exit channel barrier.

As one test of this mechanism, the experimental $P(E_T)$ distributions can be compared to prior distributions for channel (2), using a version of Eq. (11) appropriate for two diatomic fragments.[41] The comparison in Figs. 5(d)–5(f) shows that, in contrast to channel (1), the prior and experimental distributions are very different. The experimental distributions show that the fragments have considerably less translational energy, on the average, than predicted by the prior distribution. Moreover, although the 570 nm distribution peaks near $E_T=0$, the maxima in the other two distributions clearly move towards higher $E_T$ as the excitation energy is raised. More specifically, as was pointed out in Sec. IV A, the magnitude of this shift is very nearly equal to the additional excitation energy, indicating that this additional energy is efficiently channeled into product translational energy.

Taken together, these observations cast serious doubt on a statistical decomposition mechanism for channel (2). Statistical decay should lead to translational energy distributions that are, at most, weakly dependent on the excitation energy. Moreover, the high level of product vibrational excitation suggests a rather sudden dissociation beginning from a nuclear configuration in which the N–O bond lengths are very different from those in the separated products. Extensive product rotational excitation should also be expected if the nuclear configuration changes rapidly from a $C_{2v}$ structure to the trans-$ONNO^-$ intermediate on the way to products, due to the significant torque such motion exerts around the noncentral N atom of $N_2O_2^-$. A possible mechanism consistent with these results is one in which the initially prepared $N_2O_2^-$ excited electronic state interacts with another excited state that correlates asymptotically to $NO^- + NO$ products, and that dissociation to channel (2) takes place on this second excited state surface. Even though we postulate a second excited surface that is repulsive, it has been demonstrated[44] that extensive vibrational and rotational exit channel interactions, such as those qualitatively described above, can effectively channel the majority of available energy into internal states of the products.

Unfortunately, we have little information regarding what excited states may play a role in $NO^- + NO$ production. To further explore this product channel it would be useful to form ground state $ONNO^-$ in the ion source, dissociating it

at the same three wavelengths used in the current study. However, repeated attempts to create this species from the same NO/Ar mixture used in the photoelectron spectroscopy studies have not yet been successful on the fast beam translational spectrometer.

One issue raised by the mechanism proposed above is why statistical decomposition to channel (2) does not seem to be occurring, given that we believe channel (1) to proceed by dissociation from a ground state $N_2O_2^-(C_{2v})$ complex. The statistical (i.e., ground state) mechanism for channel (2) requires passage over an isomerization barrier to form the $ONNO^-$ complex, representing a much tighter transition state than that for bond fission to $O^-+N_2O$. Thus, unless the isomerization barrier is considerably lower than $D_0(O^- - N_2O)$, bond fission will dominate over isomerization once the ground state complex is formed. Unfortunately, we were unable to locate the isomerization barrier between the two potential minima in our calculations, which precludes a more quantitative analysis of the possible ground state reaction path.

### C. Comparison with photoelectron spectroscopy

The observation of both product channels shown in Figs. 4 and 5 warrants a comparison of our results to the photoelectron spectroscopy of Posey and Johnson.[7] They observe in the 532 nm photoelectron spectrum of $N_2O_2^-$ a single peak due to the detachment of $O^-$ ions. They conclude that this isomer photofragments *exclusively* to $O^-+N_2O$. At first glance, our observation of $NO^-+NO$ products at 532 nm seems to contradict their interpretation. One must question why signal from $NO^-$ photodetachment is not observed in the photoelectron spectrum if this fragment ion is in fact produced. The explanation can be found in the translational energy release distributions for channel (2) shown in the right column of Fig. 5. The small fraction of available energy in translation for this channel requires that the fragments have a high degree of vibrational excitation. Because the detachment threshold of $NO^-$ (194 $cm^{-1}$) (Ref. 22) is small compared to its vibrational frequency[45] of 1363 $cm^{-1}$, $NO^-(v>0)$ spontaneously autodetaches an electron to give primarily $NO(v'=v-1)+e^-$. The slow electrons produced from autodetachment are below the low-energy cutoff of the time-of-flight photoelectron spectrometer used by Posey and Johnson, and would not have been observed in those experiments. Taking both the photoelectron data and our translational spectroscopy experiments into account, the only mutually consistent explanation is that photodissociation of $N_2O_2^-$ at 532 nm does produce $NO^-$, but none of this product is in its ground vibrational state, and is therefore not detectable in the photoelectron spectrometer.

To further support our argument, we note that Posey and Johnson *did* observe the unmistakable photoelectron spectrum of $NO^-$ at 532 nm from photodestruction of the $ONNO^-$ isomer. As explained earlier, $NO^-$ ($v=0$) is the only product vibrational state which could produce this signal in their experiments. Therefore, if the $ONNO^-$ isomer were present in our electric discharge ion beam at any appreciable concentration, the $P(E_T)$ distributions of Fig. 5 would show some intensity at the highest possible translational energy [which corresponds to $NO^-$ ($v=0$) products]. The complete lack of intensity at these translational energies further supports our conclusion that $NO^-+NO$ arises unambiguously from $(C_{2v})N_2O_2^-$ photofragmentation.

### D. Comparison with photodissociation of $CO_3^-$

The $CO_3^-$ ion, which is isoelectronic with $N_2O_2^-$, also dissociates in the visible region, yielding $O^-+CO_2$. The photodissociation dynamics of $CO_3^-$ have been extensively examined for twenty years.[2] One might therefore expect to gain further insight into the $N_2O_2^-$ photodissociation dynamics through a comparison with the $CO_3^-$ work. The study by Snodgrass *et al.*[3] is particularly relevant for comparison to our data. They measured the $O^-+CO_2$ translational energy distribution and calculated the $CO_3^-$ geometry at the unrestricted Hartree–Fock level, finding a $^2A_2'$ ground state with $D_{3h}$ symmetry. Their translational energy distributions, like ours, peak near $E_T=0$ and decrease steadily towards higher $E_T$, indicating a high level of $CO_2$ internal excitation: However, they find that the average translational energy release *decreases* as the photon energy is increased from 514 to 476 nm, finally increasing again at 458 nm, which differs from our results and the predictions of statistical models. Based on these results, they concluded that this dissociation occurs on an excited state surface, rather than by statistical decomposition of the ground state as we have proposed for $N_2O_2^- \rightarrow O^-+N_2O$.

A closer look at both ions indicates that there are important differences in the electronic states involved in the two transitions. The visible excitation in $CO_3^-$ is assigned by Snodgrass *et al.* to the $^2E' \leftarrow {}^2A_2'$ transition. In $C_{2v}$ symmetry, the $^2A_2'$ state correlates to $^2B_2$, implying that the ground states for $CO_3^-$ and $N_2O_2^-$ have similar electronic structure. However, the $^2E'$ excited state of $CO_3^-$ correlates to a $^2A_1$ and $^2B_2$ state, neither of which corresponds to the $^2A_2$ excited state that we believe provides the oscillator strength in $N_2O_2^-$ dissociation. Instead, a $^2A_2$ state correlates to $^2E''$ in $D_{3h}$ symmetry, although the $^2E'' \leftarrow {}^2A_2'$ transition is not optically allowed. The excited states formed by electronic excitation in the two experiments are therefore quite different, which could certainly account for the different dissociation mechanisms proposed for the two anions. This comparison shows that while rough predictions about a molecule can be made based on properties of isoelectronic species, the detailed dynamics of each system can be completely dissimilar.

## VI. CONCLUSIONS

The photodissociation of $N_2O_2^-$ ($C_{2v}$) has been investigated using fast beam translational spectroscopy. Two product channels are observed: $O^-+N_2O$ and $NO^-+NO$. *Ab initio* calculations have been carried out for the lowest state of each symmetry in this ion. Based on the agreement between experiment and theory, the transition in the total dissociation cross section spectrum is assigned to $\tilde{B}(^2A_2) \leftarrow \tilde{X}(^2B_2)$.

Product state distributions for both channels show that the majority of available energy goes into internal energy of the fragments. The $P(E_T)$ distributions for channel (1) demonstrate resolved vibrational structure of the $N_2O$ fragment. From these distributions the following thermodynamic data has been derived: $D_0(O^- - N_2O) = 1.40 \pm 0.03$ eV, $D_0(N_2O_2^- \rightarrow NO^- + NO) = 1.25 \pm 0.04$ eV, and $\Delta H^0_{f,0}(N_2O_2^-) = 0.58 \pm 0.04$ eV. The calculated values from G1 and G2 theory are in good agreement with the experimental values, which lends credibility to the value calculated by the same methods (but not experimentally known) for the isomerization reaction $\Delta H_0[N_2O_2^-(C_{2v}) \rightarrow \text{trans-}ONNO^-(C_{2h})] = -0.05$ eV. Within the accuracy of the calculations, these two isomers are thermoneutral.

The formation of $O^- + N_2O$ is most consistent with a sequential mechanism of rate-limiting internal conversion to the ground state followed by fast dissociation without a barrier. At all three excitation energies used in this study, the product translational energy distributions are in overall agreement with the calculated prior distributions. However, at the lowest excitation energy, 570 nm, vibrational structure in the experimental distribution is resolved to the point where it is clear that the $N_2O$ rotational distributions are colder than predicted by the prior distribution. The $N_2O$ rotational distribution is apparently constrained by the dissociation dynamics on the ground state surface rather than by energy and angular momentum conservation. Nonetheless, because the product translational energy distributions are reasonably well predicted by a simple statistical model, we believe this channel is due to dissociation on the ground state rather than on an excited state surface.

In contrast, the translational energy distributions for the $NO^- + NO$ channel are very different from the corresponding prior distributions. Their dependence on excitation energy suggests that this channel results from dissociation on an excited state potential energy surface that interacts with the initially excited $N_2O_2^-$ $\tilde{B}(^2A_2)$ state. The translational energy distributions indicate that their is significant internal excitation of the fragments. The apparent absence of this channel in the earlier study by Posey and Johnson indicates that all of the $NO^-$ is vibrationally excited.

## ACKNOWLEDGMENTS

This research is supported by the Director, Office of Energy Research, Office of Basic Energy Sciences, Chemical Sciences Division of the U.S. Department of Energy under Contract No. DE-AC03-76SF00098. The authors wish to acknowledge several helpful discussions with Dr. Don Arnold. In addition we thank Cangshan Xu and Dr. Gordon Burton for their assistance in acquiring the photoelectron spectra in this study.

[1] L. C. Lee, G. P. Smith, J. T. Moseley, P. C. Cosby, and J. A. Guest, J. Chem. Phys. **70**, 3237 (1979).
[2] J. T. Moseley, P. C. Cosby, R. A. Bennett, and J. R. Peterson, J. Chem. Phys. **62**, 4826 (1975); J. F. Hiller and M. L. Vestal, *ibid*. **72**, 4713 (1980); D. E. Hunton, M. Hofmann, T. G. Lindeman, and A. W. Castleman, Jr., *ibid*. **82**, 134 (1985).
[3] J. T. Snodgrass, C. M. Roehl, P. A. M. van Koppen, W. A. Palke, and M. T. Bowers, J. Chem. Phys. **92**, 5935 (1990).
[4] P. C. Cosby, R. A. Bennett, J. R. Peterson, and J. T. Moseley, J. Chem. Phys. **63**, 1612 (1975); S. E. Novick, P. C. Engelking, P. L. Jones, J. H. Futrell, and W. C. Lineberger, *ibid*. **70**, 2652 (1979); J. F. Hiller and M. L. Vestal, *ibid*. **74**, 6096 (1981).
[5] C.-C. Han and M. A. Johnson, Chem. Phys. Lett. **189**, 460 (1992).
[6] C. R. Sherwood, M. C. Garner, K. A. Hanold, K. M. Strong, and R. E. Continetti, J. Chem. Phys. **102**, 6949 (1995).
[7] L. A. Posey and M. A. Johnson, J. Chem. Phys. **88**, 5383 (1988).
[8] K. Hiraoka, S. Fujimaki, K. Aruga, and S. Yamabe, J. Phys. Chem. **98**, 8295 (1994).
[9] D. E. Milligan and M. E. Jacox, J. Chem. Phys. **55**, 3404 (1971).
[10] M. E. Jacox, J. Chem. Phys. **93**, 7622 (1990).
[11] J. Hacaloglu, S. Suzer, and L. Andrews, J. Phys. Chem. **94**, 1759 (1990).
[12] M. E. Jacox, J. Chem. Phys. **93**, 7609 (1990).
[13] R. A. Moris, A. A. Viggiano, and J. F. Paulson, J. Chem. Phys. **92**, 3448 (1990).
[14] S. E. Barlow and V. M. Bierbaum, J. Chem. Phys. **92**, 3442 (1990).
[15] M. W. Chase, Jr., C. A. Davies, J. R. Downey, Jr., D. J. Frurip, R. A. McDonald, and A. N. Syverud, J. Chem. Phys. Ref. Data **14**, Suppl. No. 1 (1985).
[16] D. W. Arnold and D. M. Neumark, J. Chem. Phys. **102**, 7035 (1995).
[17] R. E. Continetti, D. R. Cyr, R. B. Metz, and D. M. Neumark, Chem. Phys. Lett. **182**, 406 (1991).
[18] R. E. Continetti, D. R. Cyr, D. L. Osborn, D. J. Leahy, and D. M. Neumark, J. Chem. Phys. **99**, 2616 (1993).
[19] D. L. Osborn, D. J. Leahy, E. M. Ross, and D. M. Neumark, Chem. Phys. Lett. **235**, 484 (1995).
[20] J. M. B. Bakker, J. Phys. E **6**, 785 (1973); *ibid*. **7**, 364 (1974).
[21] D. J. Leahy, D. L. Osborn, D. R. Cyr, and D. M. Neumark, J. Chem. Phys. **103**, 2495 (1995).
[22] M. W. Siegel, R. J. Celotta, J. L. Hall, J. Levine, and R. A. Bennett, Phys. Rev. A **6**, 607 (1972).
[23] M. A. Johnson, M. L. Alexander, and W. C. Lineberger, Chem. Phys. Lett. **112**, 285 (1984).
[24] L. G. Christophorou, D. L. McCorkle, and A. A. Christodoulides, in *Electron-Molecule Interactions and Their Applications*, edited by L. G. Chrisotophorou (Academic, Orlando, 1984), Vol. 1, pp. 477–617, and references therein.
[25] A. Thoma, B. E. Wurfel, R. Schlachta, G. M. Lask, and V. E. Bondybey, J. Phys. Chem. **96**, 7231 (1992).
[26] G. Gantefoer, H. R. Siekmann, H. O. Lutz, and K. H. Meiwes-Broer, Chem. Phys. Lett. **165**, 293 (1990).
[27] Y. Ohshima and Y. Endo, J. Mol. Spec. **153**, 627 (1992).
[28] R. Prosch and T. Trickl, Rev. Sci. Instrum. **60**, 713 (1989).
[29] R. E. Continetti, D. R. Cyr, and D. M. Neumark, Rev. Sci. Instrum. **63**, 1840 (1992). Note that only one MOSFET stage is needed for this application.
[30] S. C. Brown, *Introduction to Electrical Discharges in Gases* (Wiley, New York, 1966).
[31] D. J. Leahy, D. L. Osborn, D. R. Cyr, and D. M. Neumark, J. Chem. Phys. **103**, 2495 (1995).
[32] R. N. Zare, Mol. Photochem. **4**, 1 (1972).
[33] G. Herzberg, *Molecular Spectra and Molecular Structure, Vol. III. Electronic Spectra and Electronic Structure of Polyatomic Molecules* (van Nostrand, New York, 1966), p. 596.
[34] D. L. Osborn, D. J. Leahy, and D. M. Neumark (unpublished).
[35] GAUSSIAN 92, Revision C, M. J. Frisch, G. W. Trucks, M. Head-Gordon, P. M. W. Gill, M. W. Wong, J. B. Foresman, B. G. Johnson, H. B. Schlegel, M. A. Robb, E. S. Replogle, R. Gompets, J. L. Andres, K. Raghavachari, J. S. Binkley, C. Gonzalez, R. L. Martin, D. J. Fox, D. J. Defrees, J. Baker, J. J. P. Stewart, and J. A. Pople (Gaussian, Inc., Pittsburgh, PA, 1992).
[36] The lowest state of $C_s$ symmetry ($^2A'$) converges to the same equilibrium geometry as the ground state ($^2B_2$), and is therefore not listed as a distinct species.
[37] All experimental bond lengths for comparison with calculation are taken from J. H. Callomon. E. Hirota, T. Iijima, K. Kuchitsu, and W. J. Lafferty, *Landolt Bornstein New Series, Vol. II/15, Structure Data of Free Polyatomic Molecules*, edited by K.-H. Hellwege and A. M. Hellwege (Springer-Verlag, Berlin, 1987).
[38] J. A. Pople, M. Head-Gordon, D. J. Fox, K. Raghavachari, and L. A. Curtiss, J. Chem. Phys. **90**, 5622 (1989).

[39] L. A. Curtiss, K. Raghavachari, G. W. Trucks, and J. A. Pople, J. Chem. Phys. **94**, 7221 (1991).
[40] S. G. Lias, J. E. Bartmess, J. F. Liebman, J. L. Holmes, R. D. Levin, and W. G. Mallard, J. Phys. Chem. Ref. Data **17**, Suppl. No. 1 (1988).
[41] R. D. Levine, in *Theory of Chemical Reaction Dynamics, Vol. IV*, edited by M. Baer (CRC Press, Boca Raton, 1985), pp. 1–64.
[42] G. Z. Whitten and B. S. Rabintovitch, J. Chem. Phys. **41**, 1883 (1964).
[43] R. G. Gilbert and S. C. Smith, *Theory of Unimolecular and Recombination Reactions* (Blackwell, Oxford, 1990), Chap. 2.
[44] R. Schinke, *Photodissociation Dynamics* (University Press, Cambridge, 1993), pp. 128–132.
[45] K. P. Huber and G. Herzberg, *Molecular Spectra and Molecular Structure IV, Constants of Diatomic Molecules* (van Nostrand, New York, 1966).